

The vertical cloud structure of the West African monsoon: A 4 year climatology using CloudSat and CALIPSO

T. H. M. Stein,¹ D. J. Parker,² J. Delanoë,³ N. S. Dixon,² R. J. Hogan,¹ P. Knippertz,²
R. I. Maidment,¹ and J. H. Marsham²

Received 29 March 2011; revised 22 September 2011; accepted 23 September 2011; published 19 November 2011.

[1] The West African summer monsoon (WAM) is an important driver of the global climate and locally provides most of the annual rainfall. A solid climatological knowledge of the complex vertical cloud structure is invaluable to forecasters and modelers to improve the understanding of the WAM. In this paper, 4 years of data from the CloudSat profiling radar and CALIPSO are used to create a composite zonal mean vertical cloud and precipitation structure for the WAM. For the first time, the near-coincident vertical radar and lidar profiles allow for the identification of individual cloud types from optically thin cirrus and shallow cumulus to congestus and deep convection. A clear diurnal signal in zonal mean cloud structure is observed for the WAM, with deep convective activity enhanced at night producing extensive anvil and cirrus, while daytime observations show more shallow cloud and congestus. A layer of altocumulus is frequently observed over the Sahara at night and day, extending southward to the coastline, and the majority of this cloud is shown to contain supercooled liquid in the top. The occurrence of deep convective systems and congestus in relation to the position of the African easterly jet is studied, but only the daytime cumulonimbus distribution indicates some influence of the jet position.

Citation: Stein, T. H. M., D. J. Parker, J. Delanoë, N. S. Dixon, R. J. Hogan, P. Knippertz, R. I. Maidment, and J. H. Marsham (2011), The vertical cloud structure of the West African monsoon: A 4 year climatology using CloudSat and CALIPSO, *J. Geophys. Res.*, 116, D22205, doi:10.1029/2011JD016029.

1. Introduction

[2] The West African summer monsoon (WAM) controls the climate of the countries of sub-Saharan West Africa, and its direct influence extends eastward as far as Ethiopia. In the summer months, the WAM brings most of the annual rainfall to these countries, and therefore the WAM controls the agriculture and water resources of the local populations. In the Sahel, around 90% of the rainfall comes from the most intense, organized convective storms [Mathon *et al.*, 2002]. The WAM is also an important driver of the general circulation in the North African and Atlantic sector: for instance, the WAM interacts with the African easterly waves that pass through the region [Cornforth *et al.*, 2009; Hopsch *et al.*, 2010], which have the potential to develop into Atlantic hurricanes [Thorncroft and Hodges, 2001]. Landsea [1993] found African easterly waves to be the precursors for over 80% of intense hurricanes in the Atlantic.

[3] Despite the importance of the WAM regionally, weather and climate models have fundamental difficulty in forecasting the system. For instance, there is divergence in the

predicted rainfall for this region in the AR4 models used in the 2007 report from the Intergovernmental Panel on Climate Change (IPCC), with some models predicting a wetter climate and others predicting a drier [Intergovernmental Panel on Climate Change, 2007, section 10.3.5.2]. One reason for the uncertainty in model predictions for the region is the strong dependence of the annual climate on the surface energy balance and its interaction with dry and moist convection. For example, Tompkins *et al.* [2005a], Milton *et al.* [2008], and Rodwell and Jung [2008] showed that there is a strong sensitivity in the regional dynamics to the radiative impact of dust aerosol, and we expect a similar sensitivity to cloud-radiative processes. A strong dependence of model bias on convective cloud cover was found by Allan *et al.* [2007], who used data from the Geostationary Earth Radiation Budget (GERB) data to evaluate the Met Office global forecast model, but lack of information on the vertical cloud structure leads to uncertainty in the interpretation of these results.

[4] There have been a number of satellite studies of the cloud distributions associated with the WAM, including definitive analysis of Meteosat infrared distributions published by Duvel [1988, 1989] and systematic analysis of cloud systems making use of data from the Tropical Rainfall Measuring Mission (TRMM) [Fink and Reiner, 2003; Mohr, 2004; Mohr and Thorncroft, 2006; Laing *et al.*, 2008]. The Meteosat cold cloud results have explained much of the

¹Department of Meteorology, University of Reading, Reading, UK.

²Institute for Climate and Atmospheric Science, School of Earth and Environment, University of Leeds, Leeds, UK.

³LATMOS/IPSL/UVSQ, Guyancourt, France.

convective activity in the region according to climatological zone and topography, and the combination with TRMM has helped to quantify the links between rainfall and synoptic state. However, these satellite sensors are not able to explain the vertical structure of clouds, especially nonprecipitating clouds, in much detail. For instance, *Geerts and Dejene* [2005] used 5 years of TRMM data to analyze the vertical structure of precipitation systems, but the TRMM precipitation radar sensitivities limited their study to storms larger than about 10 km², while its inability to detect light snow and ice prevented the distinction between congestus and weakly precipitating stratiform systems.

[5] On the basis of a short aircraft research campaign, JET2000 [*Thorncroft et al.*, 2003], *Parker et al.* [2005a] described the distribution of various clouds in the WAM system and noted the prevalence and importance of various nonprecipitating types, including shallow cumulus, cumulus congestus, and a significant layer of altocumulus at the top of the Saharan air layer (SAL, around 500 hPa). These nonprecipitating clouds are important to the radiative energy balance of the regional climate, as well as to the redistribution of water vapor in the WAM, but they are poorly observed by ground-based or satellite systems. In this paper, we use 4 years of observations of cloud and precipitation from the CloudSat profiling radar (CPR) [*Stephens et al.*, 2002] and the Cloud-Aerosol Lidar and Infrared Pathfinder Satellite Observation (CALIPSO) [*Winker et al.*, 2003] to present a comprehensive study of the cloud and precipitation vertical structure during the WAM.

[6] A key feature of the WAM is the African easterly jet (AEJ), which results from the low-level temperature gradient between the Gulf of Guinea and the Sahara [*Thorncroft and Blackburn*, 1999]. Since it is to first order in thermal wind balance and has a dynamical influence on convective and synoptic weather systems, the AEJ is widely used as a diagnostic for the WAM.

[7] Several cloud types can be expected to vary in occurrence in relation to the jet position, such as a lack of low-level cloud just north of the AEJ where the monsoon layer ends [*Parker et al.*, 2005a], or fewer, but more intense and more intermittent, deep convective systems directly north of the jet [*Mohr and Thorncroft*, 2006]. Other clouds such as cirrus, congestus, and altocumulus may have similar associations with the AEJ, with impacts on radiation and precipitation, and these can now be readily characterized using CloudSat and CALIPSO.

[8] Launched in 2006, CloudSat and CALIPSO provide detailed information on the vertical structure of clouds throughout the atmosphere. In their sun-synchronous orbit as part of the A-Train, the pair make roughly 32 equatorial overpasses each day, at approximately 01:30 and 13:30 local time (LT). The synergy between radar and lidar allows for improved cloud observations, with the lidar sensitive to smaller ice crystals in cirrus and near cloud top, and with the radar's ability to penetrate most deep convective clouds and precipitation through to the surface [*Delanoë and Hogan*, 2010]. Their sensitivity and vertical scanning ability allows for the detection of all but the thinnest of cloud types [*Mace et al.*, 2009].

[9] The aim of this paper is therefore to describe the mean state of the cloud structures in the WAM system, making use of 4 years of CloudSat and CALIPSO data. In section 2,

the cloud target classification method by *Delanoë and Hogan* [2010] and the merging of CloudSat-CALIPSO data are explained. A cloud-type classification for individual CloudSat-CALIPSO profiles is introduced in section 2.2, and the locating procedure of the AEJ position in the European Centre for Medium-Range Weather Forecasts (ECMWF) Operational Analyses is described in section 2.3. Past studies on precipitation, moisture, and radiation during the WAM have highlighted the zonal structure of the regional variability [*Hamilton and Archbold*, 1945; *Duvel*, 1988; *Meynadier et al.*, 2010]. The results are therefore presented in terms of zonal means of cloud fraction (section 3) and frequency of events and amount when present (section 4). Observations of individual cloud types are discussed in section 5 with the supercooled liquid cloud fraction in altocumulus clouds presented in section 6. In section 7, statistics of convective cloud are shown relative to the AEJ position. These results will be valuable to forecasters in presenting cloud-type statistics according to latitude and AEJ. Moreover, we present a benchmark cloud structure against which numerical models for the regional weather and climate can be tested and improved.

2. Data and Methods

[10] In this section, the model and data products used for the analysis are discussed. The period of observation and model data covers the months June–September to encompass the WAM season and active periods with wave disturbances of the AEJ. The analysis is performed for the years 2006–2009, given the CloudSat and CALIPSO launch date in April 2006 and the availability of the “DARDAR-MASK” product.

2.1. Description of the DARDAR-MASK Product

[11] Part of the A-Train constellation of satellites, CloudSat and CALIPSO provide high-resolution vertical cloud profiles across the globe, with a return period of approximately 16 days [*Stephens et al.*, 2002]. To facilitate joint analysis, the lidar and radar data have been merged on to the same grid [*Delanoë and Hogan*, 2010] in the DARDAR-MASK product. The 94 GHz CPR provides vertical profiles of equivalent radar reflectivity factor at approximately 1.5 km horizontal and 240 m vertical resolution. CALIPSO provides apparent lidar backscatter at 333 m horizontal resolution and at a variable vertical resolution of 30 to 60 m in the troposphere. CPR reflectivities are linearly interpolated from their 240 m vertical resolution on to a regular 60 m grid, while the lidar signal is averaged horizontally on to the CloudSat 1.5 km horizontal grid before being averaged up to the regular 60 m vertical grid. The “ECMWF-AUX” product [*Partain*, 2007] contains temperature and pressure provided by the European Centre for Medium-Range Weather Forecasts (ECMWF) from their global model short-range forecasts on the CloudSat track and grid, which are interpolated similar to the CPR reflectivities on to the 60 m vertical grid; hence all data in the DARDAR-MASK product are available on a regular 1.5 km grid with 60 m vertical resolution.

[12] In the DARDAR-MASK, the CloudSat cloud mask from the “2B-GEOPROF” product [*Marchand et al.*, 2008] is used to determine hydrometeor occurrences when its value located nearest to the merged grid is above 20 (arbitrary

units), which indicates confidence in hydrometeor detection. Additionally, CALIPSO observations are included in the target classification by taking the value located nearest to the merged grid from the “Lidar Level 2 Vertical Feature Mask” [Anselmo *et al.*, 2006], which uses the five categories “clear air,” “cloud,” “aerosols,” “surface,” and “no signal.” Subsequently, the values inherited from the CloudSat and CALIPSO masks on the merged grid are checked for consistency with CPR reflectivity and lidar attenuated backscatter. The Delanoë and Hogan [2010] target classification has its own supercooled water identification method, based on the strong backscatter signal received by the lidar when supercooled droplets are present in the cloud. For such observations, when the CPR reflectivity is near or below the sensitivity threshold of -28 dBZ, the target is classified as supercooled liquid cloud, whereas when higher reflectivities are observed, the target is classified as a mixture of ice and supercooled liquid.

[13] Unfortunately, the current CALIPSO cloud masks are unable to distinguish between ice cloud and aerosol efficiently and accurately [Ben-Ami *et al.*, 2009], which may lead to spurious cloud observations. Over the Sahara, dust may be lifted to temperatures colder than 0°C , so we exclude any lidar-only observations of ice-only cloud at temperatures warmer than -25°C , under the assumption that nearly all ice-only clouds at those temperatures are observed by the radar [Stein *et al.*, 2011]. To prevent confusion between dust (or smoke) and liquid cloud, any lidar-only observations for $T \geq 0^{\circ}\text{C}$ with total attenuated backscatter at 532 nm less than $10^{-5}\text{ m}^{-1}\text{ sr}^{-1}$ are set to “clear” and will not be included in the cloud and precipitation statistics. Ground clutter is dealt with by removing observations in the first 600 m above the ground level in the merged product. Some cloud and precipitation may not be detected by the combined CloudSat and CALIPSO masks, for instance when the lidar signal is extinguished by optically thick anvil above optically thin clouds that are below the CPR reflectivity threshold. Heavy precipitation systems may also affect the CPR reflectivities due to multiple scattering and attenuation. Battaglia *et al.* [2008] found that while only 0.3% of oceanic profiles identified as raining have the CPR signal attenuated beyond the sensitivity threshold before reaching the surface, 25% of raining oceanic profiles in the tropics were affected by multiple scattering. In heavy precipitation, multiple scattering enhances CPR reflectivities and may partially compensate for attenuation, often producing an apparent reflectivity signal down to the surface [Battaglia *et al.*, 2008], but which is not quantitatively related to the properties of the hydrometeors at that height. In this paper, however, reflectivities are only used qualitatively to indicate the presence of hydrometeors. Clouds in which the multiple scattering return extends all the way down to the surface are invariably those producing heavy precipitation that reaches down to the surface as well. Therefore, no treatment for either attenuation or multiple scattering is needed for this qualitative analysis. Finally, the CPR and CALIPSO have no direct capability of distinguishing falling hydrometeors (rain and snow) from those suspended in the cloud, while the Delanoë and Hogan [2010] method contains a “rain” flag based on reflectivity. For the purpose of this paper, we will include observations of both cloud and rain, so that we obtain

the vertical structure of combined cloud and precipitation features.

[14] The period of observation from June–September of 2006–2009 includes 5,505 orbits from CloudSat and CALIPSO. The cloud and precipitation climatologies in this paper are composites from 957,515 nighttime and 836,926 daytime profiles sampled in the region 10°W – 10°E and 0°N – 30°N . The pressure and temperature data used to bin the cloud statistics are from the ECMWF-AUX product interpolated on to the merged grid. Due to the small footprint and long return period, the use of CloudSat and CALIPSO observations to study convection triggered by orography is limited. The same shortcomings of these satellites limit their use in studying synoptic variability of the AEJ. Therefore, the results in this paper are primarily presented in terms of zonal and seasonal means.

2.2. Cloud-Type Classification

[15] With some limitations, we can distinguish between different cloud types using the DARDAR-MASK. For this purpose, we treat each CloudSat-CALIPSO profile independently and define a layer as a vertically continuous region where hydrometeors are detected by at least one of the instruments. This layer is then assigned a single cloud type as follows: (1) shallow cloud, with layer top pressure larger than $0.7p_s$, where p_s is the pressure at 600 m above ground; (2) congestus, with layer top pressure larger than 350 hPa and extending down to pressures of $0.9p_s$; (3) mid-level cloud, layers with pressures between 350 hPa and $0.7p_s$; (4) cumulonimbus, with layer top pressure smaller than 350 hPa and extending down to pressures of $0.9p_s$; (5) anvil, with layer top pressure smaller than 350 hPa and base between 200 hPa and $0.9p_s$; and (6) cirrus, layers located at pressures below 200 hPa.

[16] Note that these cloud-type names are used for simple identification and that categories may include other cloud types. “Anvil,” for instance, will include virga and clouds located below the 200 hPa, while “cumulonimbus” will include nimbostratus. Although these categories, and the thresholds which define them, have been selected subjectively, they do correspond to distinct separations in the cloud statistics and forms observed.

[17] In particular, it is found that the freezing level in the WAM region lies around the top of the SAL (to be discussed later), and therefore the 350 hPa threshold separates altocumulus formed at the top of the SAL from clouds with substantially colder tops. Note that this classification does not depend on the horizontal extent of a cloud layer, nor does it take into account optical thickness or maximum reflectivity, which are key to the more sophisticated approach by Wang and Sassen [2007], although they currently do not make use of CALIPSO observations.

2.3. African Easterly Jet Location

[18] The AEJ position was calculated from ECMWF Operational Analyses (ECMWF, the description of the ECMWF/WCRP Level III-A Global Atmospheric Data Archive, 1995), for every 1.0° longitude and at 1.0° latitude resolution, for every 6 hours from 00:00 to 24:00 UTC. To determine the jet position, first the search was restricted to latitudes between 5°N and 20°N and within those latitudes to the region where temperatures at 850 hPa were between

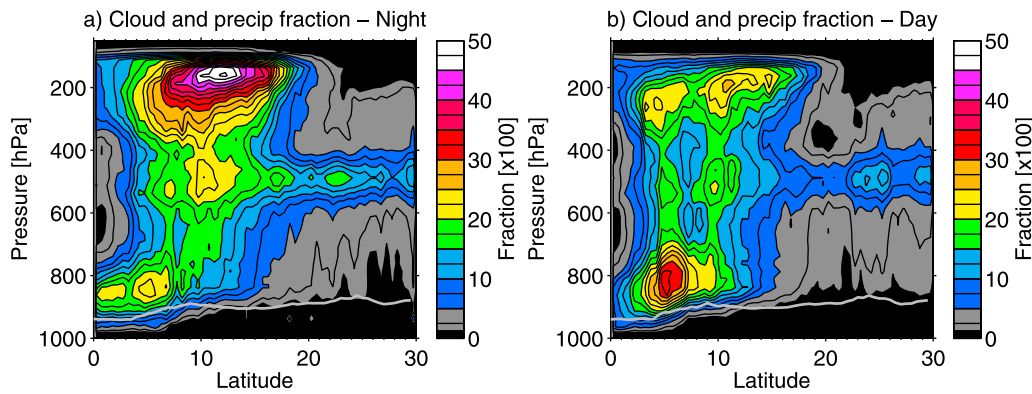


Figure 1. Cloud and precipitation fraction for June–September 2006–2009 observed by CloudSat and CALIPSO for (a) nighttime overpasses and (b) daytime overpasses. Fractions are shown at 2.5% intervals at a resolution of 0.5° in latitude and 25 hPa in pressure, averaged over all observations throughout the period between 10°W and 10°E . Values below 1.25% are shown in black with a thick gray line indicating the mean pressure at 600 m above the surface.

292 K and 298 K, to prevent confusion with other local wind speed maxima. Within this region, for each degree longitude the jet location was then defined by the location of maximum full wind speed at 700 hPa, rounded to the nearest degree in latitude. Both temperature and wind fields were smoothed using a moving average with a box size of 7×7 data points (i.e., degrees) to remove any sharp variations in these fields and the resulting jet latitude.

[19] The AEJ location is used to calculate the dynamic latitude of a CloudSat–CALIPSO profile, that is its position in latitude relative to the jet. For each 0.5° latitude section of the CloudSat–CALIPSO track, we find the mean jet location for the longitudes of this transect. The mean jet location is then subtracted from the CloudSat–CALIPSO latitudes to give us the dynamic latitude used in section 7.

[20] A case study by Thorncroft *et al.* [2003] from the JET2000 project showed an AEJ in the ECMWF analysis within 1° of the jet latitude observed with dropsondes. Using another case study from the same project, Tompkins *et al.* [2005b] showed that the AEJ in the ECMWF analysis does not compare as well with dropsonde measurements in the presence of mesoscale convective systems, due to poor representation of such events in the model. Agustí-Panareda *et al.* [2010] evaluated ECMWF analyses with and without assimilation of the extra radiosondes from the African Monsoon Multidisciplinary Analysis (AMMA) project [Redelsperger *et al.*, 2006]. Both model versions showed reasonable agreement with Meteosat-8 atmospheric motion vectors for the jet location between 10°W and 10°E when compared on a $2^\circ \times 2^\circ$ grid, but tended to produce a weaker jet at its entrance east of 10°E , which would impact the model's ability to forecast African easterly waves. Despite the model's shortcomings in representation of synoptic variability of the AEJ, the accuracy in determining the location of the AEJ is sufficient for the purpose of this study.

3. Zonal Mean Vertical Cloud Structure

[21] In Figure 1, the cloud and precipitation fraction with pressure is shown zonally averaged between 10°W and 10°E for June–September of 2006–2009. Maximum cloud fractions of about 50% are found at nighttime for pressures

lower than 200 hPa and between 8°N and 16°N . For daytime observations, the cloud fractions at these pressures are much lower, with a maximum of about 25% at 11°N . This latitude range is typically associated with the rainfall maximum during the West African monsoon [Mathon *et al.*, 2002; Sultan and Janicot, 2003a, 2003b], and these cloud occurrences can be interpreted as cirrus and anvil resulting from deep convection. Two columns of enhanced cloud and precipitation fractions occur for nighttime observations at 7°N and 9°N – 12°N and for daytime observations at 5°N and 10°N . Comparing this result with the locations of convective systems by Mohr and Thorncroft [2006], these columns can be associated with higher occurrences of convective systems over the Cameroon Highlands at 5°N – 7°N and the Jos Plateau at 10°N . A secondary maximum between 4°N and 16°N occurs near 500 hPa, indicative of a congestus and cumulonimbus detrainment layer around the freezing level [Johnson *et al.*, 1999].

[22] Daytime maximum fractions above 30% are observed for low-level cloud and precipitation, located at 5°N – 7°N , with values above 20% found as far north as 10°N , indicating the advance of the monsoon layer in the early afternoon. For nighttime observations, these fractions only reach up to 7°N , although a secondary maximum is observed over the Gulf of Guinea between 0°N and 3°N . Parker *et al.* [2005b] and Lothon *et al.* [2008] have shown how low-level advection of moisture is maximized in the nighttime hours, and it is likely that the northward advection of moisture overnight supports a maximum northward extent of low-level cloud persisting until 13:30 LT, while drying through entrainment of dry air in the planetary boundary layer (PBL) in the afternoon erodes the low-level cloud later in the day [Hamilton and Archbold, 1945].

[23] North of 15°N , a layer of relatively high cloud fraction is found at pressures near 500 hPa, with values up to 20% at night and up to 15% during the day. These clouds are at the top of the SAL (as noted by Parker *et al.* [2005a]) and may locally be linked to orographic features such as the Hoggar mountains at 23°N . Their cloud-top temperatures are generally below freezing, but do not necessarily show ice formation [Ansmann *et al.*, 2008]. As noted in section 3, this cloud layer at 500 hPa stretches as far south as 4°N ,

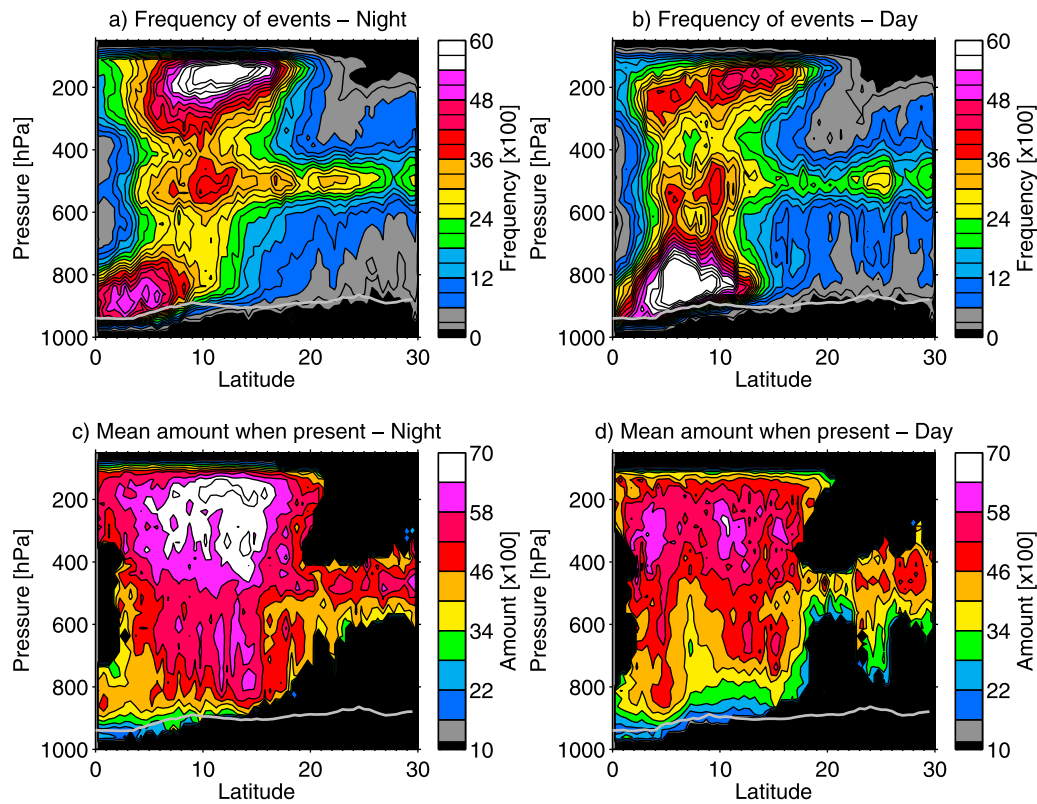


Figure 2. (a–b) Cloud and precipitation frequency of events of fractions 10% and higher, for June–September 2006–2009 observed by CloudSat and CALIPSO for nighttime overpasses (Figure 2a) and daytime overpasses (Figure 2b). (c–d) Mean amount when present, i.e., the mean cloud and precipitation fraction over all events with fraction 10% and higher for nighttime overpasses (Figure 2c) and daytime overpasses (Figure 2d). Fractions are calculated for each orbit at a resolution of 0.5° in latitude and 25 hPa in pressure, with frequencies and mean amounts averaged over all observations throughout the period between 10°W and 10°E . A thick gray line indicates the mean pressure at 600 m above the surface.

although it is important to note the possibly different origins of clouds (altocumulus versus detrainment from congestus and cumulonimbus) in this layer.

[24] There is a clear distinction between the daytime and nighttime organization of clouds, with a dominant feature of shallow cumulus and congestus in the early afternoon, while deep (convective) cloud and the associated anvils and cirrus dominate the nighttime structure. The diurnal cycle and evolution of congestus into cumulonimbus cannot be readily observed using CloudSat and CALIPSO, but brightness temperatures have been used in combination with CloudSat data to help determine which of the daytime congestus features are buoyant and may develop into cumulonimbus [Luo *et al.*, 2009].

4. Frequency of Events and Amount When Present

[25] In this section, we expand the statistics of the cloud fractions presented in section 3 into cloud frequency and spatial extent. For every individual orbit, we calculate cloud volume fractions from the CloudSat–CALIPSO data over a typical climate model resolution of 0.5° latitude by 25 hPa. We then impose a cloud volume fraction threshold to denote an “event” and calculate the frequency of events, as well as the mean cloud volume fraction for those events, that is the

mean amount when present. Given the roughly 30 CloudSat–CALIPSO profiles per 0.5° latitude, we set the cloud volume fraction threshold to 10%, so that a deep convective cloud layer filling any 25 hPa range would be picked up by this statistic if it stretched over three consecutive profiles (about 5 km wide). At lower levels, the 25 hPa range translates to roughly 250 m, so that a single low-level cloud of 100 m depth is required to occur over 12.5 km to be classified as an event. Similarly, at 200 hPa the 25 hPa range translates to roughly 1 km, so that a 200 m thick layer of cirrus or anvil is required to stretch over 25 km before it is picked up by the 10% threshold. Note also that we do not require the hydrometeor occurrences to form a contiguous layer over the 0.5° latitude by 25 hPa range, though we expect the contribution due to random noise to be minimal given the processing in the 2B-GEOPROF mask [Marchand *et al.*, 2008].

[26] The frequency of events is presented in Figures 2a and 2b for nighttime and daytime observations, respectively, with the corresponding mean amounts when present in Figures 2c and 2d. High frequencies of events are present for both daytime and nighttime observations for low-level clouds ($p > 700$ hPa) between 0°N and 13°N , which during the day reaches values above 60% from the coast at 5°N northward up to 10°N , while at night maximum values

around 50% are observed stretching southward from the coast over the Gulf of Guinea. This nighttime stratiform cloudiness was also observed for the WAM by *Schrage et al.* [2007] using radiosonde observations and was connected to large-scale flows and the configuration of the AEJ. Daytime frequency contours for low-level cloud can be seen to lie farther north than at night, again indicating the development of the monsoon layer into the early afternoon and the erosion of low-level cloud later in the day. The low-level clouds between 0°N and 13°N have mean amounts when present below 52%, suggesting that the clouds in the monsoon layer may appear regularly, but are not abundant when present on a scale of 0.5° latitude.

[27] A second nighttime maximum frequency is present for cirrus and anvil clouds at pressures around 200 hPa and latitudes 7°N–16°N, reaching values over 60% and mean amount when present of 64% and higher. During the day, values at 200 hPa are reduced to frequencies around 40% and mean amounts below 60%. This pattern, with cirrus and anvil more frequent and extensive at 01:30 LT than at 13:30 LT, is consistent with the observation that the diurnal peak in deep convection, which presumably feeds these clouds, has its peak in the evening, before 01:30 LT, and its minimum in the morning, before 13:30 LT [*Hodges and Thorncroft*, 1997]. A maximum for midlevel cloud events reaching frequencies of around 30% during the night and around 24% during the day can be distinguished north of 15°N and is recognizable as a local maximum as far south as 4°N. These clouds at the top of the SAL have mean amounts around 54% at night (46% during the day), which combined with the frequency of events suggests some regularity and coherence and agrees with the cloud fractions of up to 20% (15%) in Figures 1a and 1b.

[28] The night-day contrast is again clear from Figures 2a and 2b, with high frequencies of low-level and congestus clouds around midday, while cumulonimbus and the resulting anvil and cirrus dominate the nighttime frequencies. This contrast appears less obvious in Figures 2c and 2d, where daytime mean amounts are generally lower than at night, apart from an increase of low-level mean amount around 5°N. High frequencies are not necessarily associated with huge cloud amounts, or vice versa, as we can imagine from fractured shallow cumulus fields, or mesoscale convective systems that occur during the WAM. Finally, high mean cloud amounts at around 350 hPa (typically not a level of detrainment) during the night indicate that the deep convective systems dominating this pressure range at this time have developed into large systems, while the lower mean amounts at this pressure during the day indicate that systems are less extensive and/or have not yet reached a mature cumulonimbus stage. Interestingly, the maximum mean amounts at this 350 hPa level occur directly north of the region of maximum frequency of events (and also south at 4°N during the day) implying that only less-frequent but large convective systems are supported in these fringe regions [*Mohr and Thorncroft*, 2006].

5. Occurrence of Individual Cloud Types

[29] Although we may infer cloud-type occurrences from Figures 1 and 2, the contribution from individual cloud layers and types to these statistics are masked in Figures 1

and 2. For instance, there is a hint of congestus occurrence during the day at 5°N and 10°N, but this cannot clearly be distinguished from a combination of shallow and midlevel clouds in Figures 1 and 2. In Figures 3, 4, and 5, we show contours of cloud fractions from the subsets of profiles described in section 2.2, at a resolution of 0.5° in latitude and 25 hPa in pressure for a direct comparison with Figures 1 and 2. The cloud fraction of 5% for these contours is chosen so that frequent events with low mean amounts such as the low-level cloud reaching 14°N or daytime altocumulus in Figure 2b still appear in this analysis. Contours of potential temperature are shown for comparison of cloud locations with features such as the monsoon layer and the SAL discussed by *Parker et al.* [2005a], while meridional wind and omega vectors show the mean circulation and a separate contour indicates the mean AEJ location. The potential temperature and wind data are the monthly and seasonal means at 00:00 UTC (nighttime) and 12:00 UTC (daytime) between 10°W and 10°E from the ECMWF Re-Analysis (ERA-Interim) [*Dee et al.*, 2011], averaged over the years 2006–2009 keeping the ERA-Interim pressure levels and horizontal resolution, with winds subsequently averaged to a regular 2° latitude by 50 hPa grid. No sampling of the ERA-Interim data along the CloudSat-CALIPSO track was attempted as these data are included to provide a picture of the mean state of the atmosphere during the WAM.

[30] The nighttime analyses in Figures 3a, 3c, 4a, 4c, and 5a show that most of the nighttime cirrus and anvil occur in the same region as deep convection as expected, while the anvil generally extends farther south over the Gulf of Guinea than the cirrus layer. Given our distinction between cirrus and anvil, the former would be produced by the most intense convective systems, which tend to follow the seasonal cycle of the AEJ position [*Mohr and Thorncroft*, 2006], although enhanced cirrus over Africa has also been linked to planetary wave activity [*Virts and Wallace*, 2010]. Particularly during the day, higher cirrus fractions (indicated by the 10% cloud fraction contour) are seen to extend north of the area with deep convection, while the anvil is still centered on the region where cumulonimbus occurs, although with a smaller spread than during the night.

[31] Interestingly, anvil is also observed in June and September north of 25°N, possibly related to convection over the Atlas mountains. Analysis of direct association between these different cloud types would help clarify the origin of cirrus and anvil, but is impractical using only the narrow-track CloudSat-CALIPSO data.

[32] The overall northward shift of congestus and cumulonimbus with the WAM and AEJ from June to August is clear in Figures 3 and 4, with a weak southward retreat in these convective clouds during the monsoon retreat in September. The occurrence of cumulonimbus extends just north of the AEJ core, although cloud fraction does not capture the rarest events that occur farther north of the AEJ, shown by *Mohr and Thorncroft* [2006, Figure 7] as well as in Figure 7 in section 7. Daytime convection occurs in regions of large-scale low-level ascent. Nighttime convection occurs farther north in regions of daytime ascent, but at night these are often regions of average descent, except in September. For all months, the deep convective activity occurs farther north than the peak in congestus occurrence,

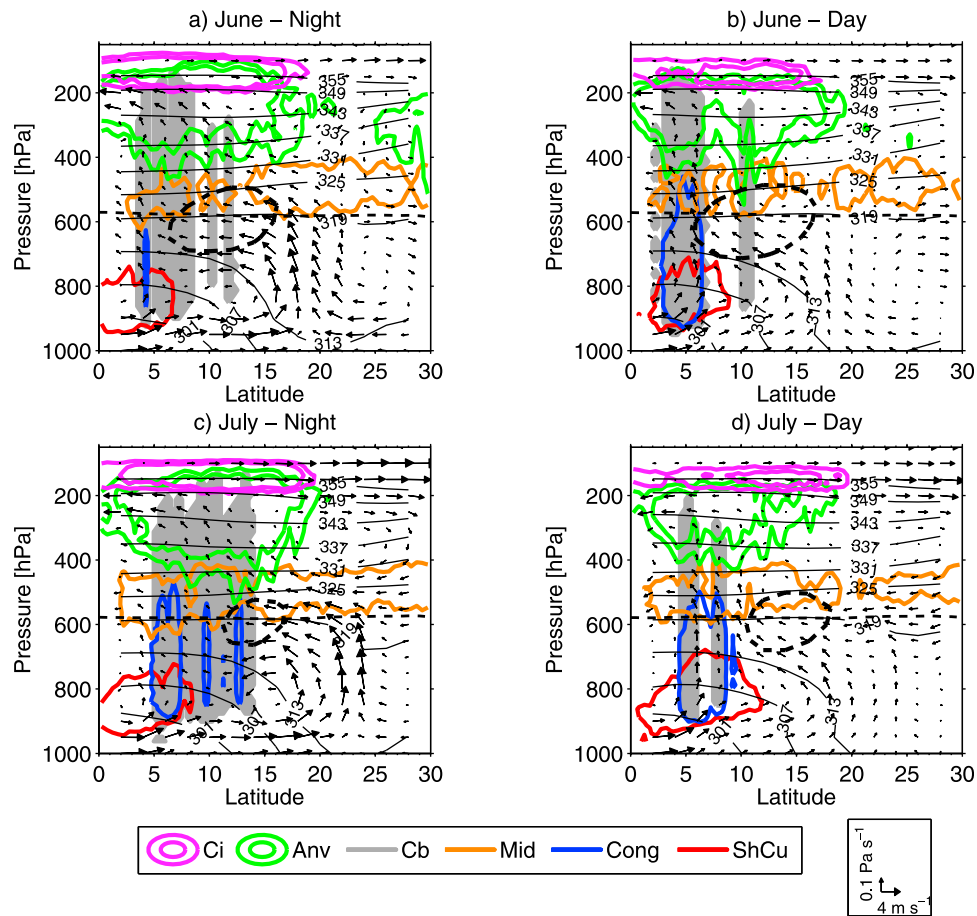


Figure 3. Contours of cloud and precipitation fraction for different cloud-type subsets for (a and b) June nighttime and daytime and (c and d) July nighttime and daytime. Contours enclose cloud fractions for cirrus (cloud fraction above 5% and 10%, magenta), anvil (5% and 10%, green), altocumulus (5%, orange), congestus (5%, blue), shallow cumulus (5%, red), and cumulonimbus (5%, shaded gray). A dashed line indicates the melting layer, and thin lines indicate contours of potential temperature at 6 K intervals. The dashed contour encloses zonal winds less than -10 m s^{-1} to indicate the AEJ position. Wind vectors are scaled to give 12 h advection distance.

indicating a different distribution of intense convective systems compared with weaker systems and congestus in this region, in line with *Mohr and Thorncroft* [2006]. This difference is largest in June, when the variation in the AEJ is largest, with cumulonimbus extending 6° north of the congestus, compared with only 1° in August. June is the month of the WAM onset, typically occurring late in the month [*Sultan and Janicot*, 2003b]. Around this time, the nocturnal winds are particularly coherent and dominate the moisture budget in the Sahel [*Lothon et al.*, 2008], suggesting that the northward extension of the nocturnal cumulonimbus in June may be fed by these strong nocturnal flows [*Sultan et al.*, 2007]. The occurrence of intense convection in the dry atmosphere of the northern Sahel in June may also favor dust generation by cold pool outflows at this time [*Marshall et al.*, 2008].

[33] Midlevel cloud can be seen to occur throughout the region, although its southernmost extent seems to be defined by the detrainment of congestus and cumulonimbus. This midlevel cloud occurrence is typically found at temperatures below freezing and centered around the 325 K potential

temperature contour. The Saharan altocumulus should be of particular interest to climate modelers, as these cloud occurrences will affect radiation budget calculations, while their microphysical properties will be affected by the presence of dust [*Ansmann et al.*, 2008].

6. Occurrence of Supercooled Liquid Water in Midlevel Clouds

[34] Although the study of specific ice and liquid water content retrievals lies beyond the scope of this paper, the occurrence of supercooled liquid is a first-order indication of the type of cloud physics involved, particularly in altocumulus over the Sahara. In Figure 6a we show the fraction of profiles with midlevel cloud per 0.5° latitude. Their occurrence is common during night and day with a fraction of about 20% north of 5°N (that is, the Gulf of Guinea coastline; compare Figure 1). Also shown in Figure 6a is the fraction of profiles that contain midlevel cloud with supercooled liquid anywhere in the top 240 m of the cloud layer,

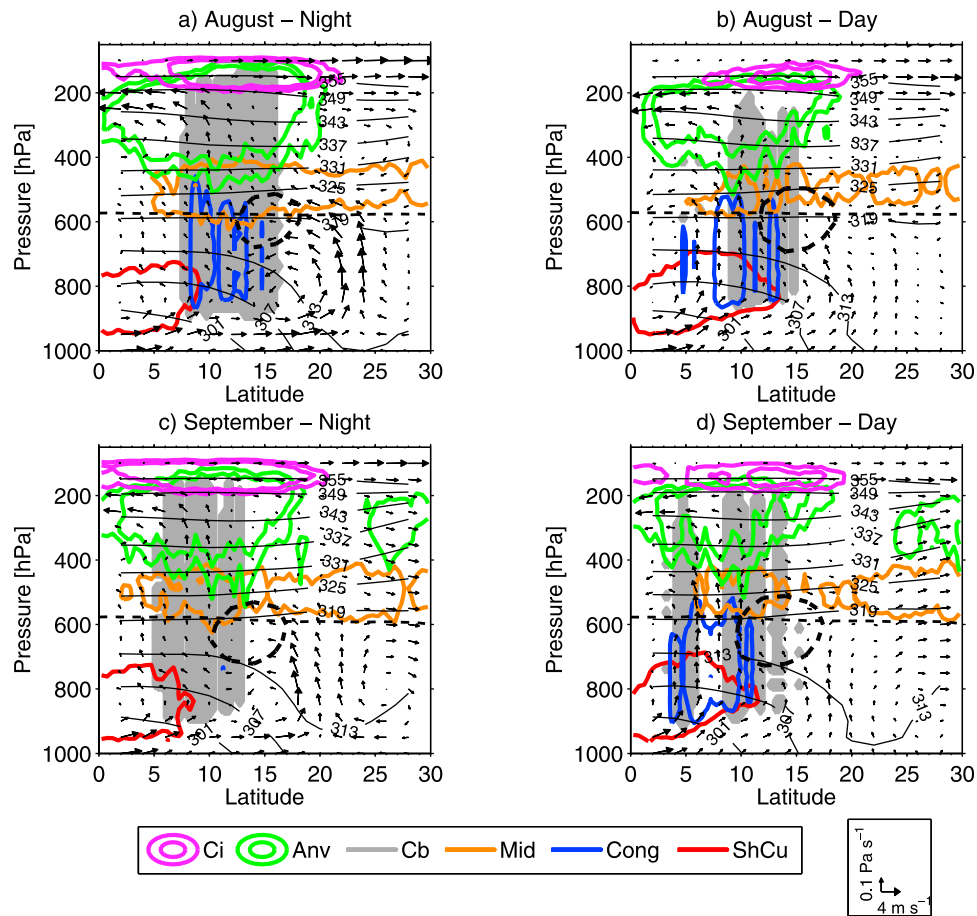


Figure 4. Same as Figure 3 but for (a and b) August nighttime and daytime and (c and d) September nighttime and daytime.

where supercooled liquid is identified using the *Delanoë and Hogan* [2010] method.

[35] The remainder of the profiles either have an ice-only top, but may contain supercooled liquid elsewhere in the

layer, or the target has not been identified due to extinction of the lidar signal (these profiles are still included in the “all” midlevel cloud probability). Clearly, the majority of mid-level cloud observed during the WAM contains supercooled

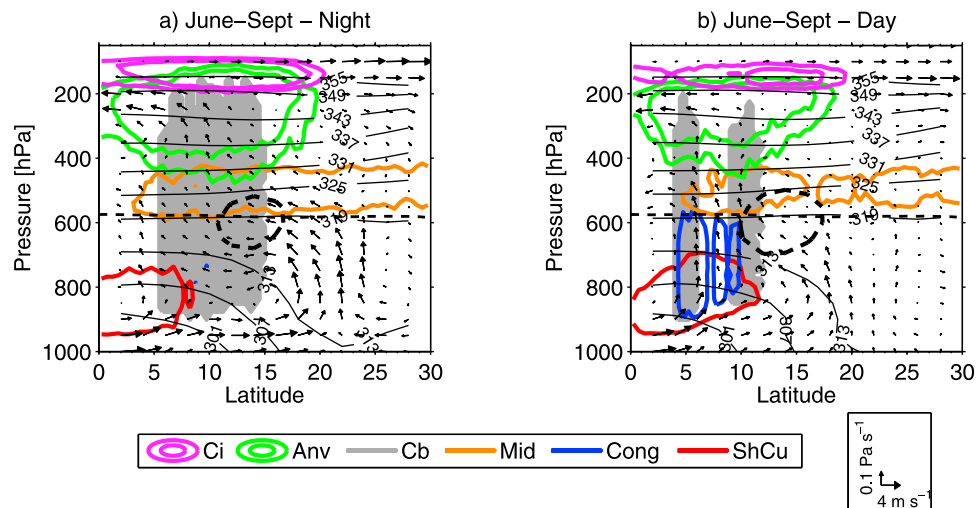


Figure 5. Same as Figure 3 but for the WAM season June–September (a) nighttime and (b) daytime.

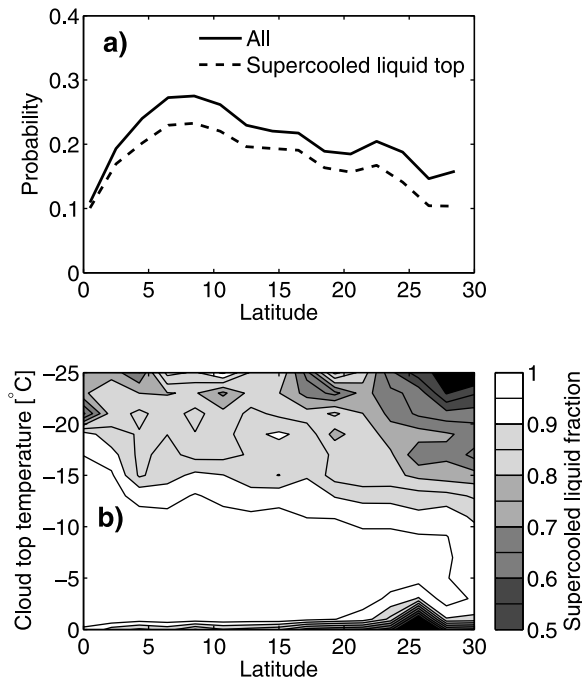


Figure 6. (a) Probability of a profile with midlevel cloud versus latitude; dashed line indicates the probability of midlevel cloud with supercooled liquid water anywhere in the top 240 m. (b) Probability of supercooled liquid in the cloud top per 2°C and 2° latitude.

liquid in the cloud top (assuming the number of profiles with multiple midlevel clouds is negligible).

[36] The distinction between supercooled liquid and ice-only cloud tops for midlevel clouds is stratified by temperature in Figure 6b, where we have excluded tops for which the hydrometeor phase could not be determined. Note that the 350 hPa level that is used to distinguish midlevel cloud from anvil corresponds to roughly -25°C , comparable to the minimum temperature at which Hogan *et al.* [2004] observed supercooled liquid in clouds between 0°N and 30°N with the Lidar In-space Technology Experiment (LITE). For all latitudes, given a cloud-top temperature warmer than -15°C , there is at least a 85% probability of observing supercooled liquid. This is consistent with results from Ansmann *et al.* [2008], who did not observe ice formation in supercooled liquid clouds over southern Morocco when cloud tops were warmer than -15°C . For cloud-top temperatures colder than -15°C , the probability of supercooled liquid in the cloud top reduces to about 50% at -5°C , most notably northward over the Sahara. This agrees with results from Westbrook and Illingworth [2011] who used radar and lidar observations from the Chilbolton Observatory in the United Kingdom and found that at least 50% of ice clouds with tops warmer than -27°C were liquid topped.

[37] The existence of supercooled liquid clouds in the layer just above the freezing level presents a number of stimulating scientific questions. We can note that the freezing level coincides with the top of the SAL (Figures 3, 4, and 5), a layer which is commonly dust laden [Cuesta *et al.*, 2009], and the presence of dust, acting as ice nuclei might be expected to cause freezing of supercooled water [Ansmann *et al.*, 2008]. Furthermore, the coincidence of the

freezing level with the upper limit of the SAL is itself an intriguing coincidence: we can ask the question whether there is a thermodynamic cause to this link.

[38] As noted by Betts [1986] and Johnson *et al.* [1996], the freezing level is on average a cold point of the tropical profile, and this phenomenon was confirmed for the SAL in the case study of Parker *et al.* [2005a]. The presence of a cold point in the ambient profile may act as a natural limit to the upward growth of the Saharan convective boundary layer, especially if reinforced by cloud microphysical thermodynamics. However, the further exploration of this idea would require careful modeling studies.

7. The African Easterly Jet and Its Dynamic Control on Convection

[39] The cloud structures presented thus far are not simply controlled by a preference for particular latitudes. The progression of the monsoon can be followed in Figures 3 and 4 with cumulonimbus and congestus occurring farther inland as the season continues: this simple north-south progression of the WAM through the annual cycle was presented in a basic synoptic model by Hamilton and Archbold [1945]. Furthermore, Newell and Kidson [1984] showed that changes in the regional rainfall can be related to a shift in the latitudinal position of the seasonal mean AEJ. In this section, we study whether the progression of cumulonimbus and congestus clouds can be coherently related to the position of the AEJ and if we can quantify this relationship.

[40] Note that the zonal mean vertical cloud and precipitation structure versus dynamic latitude (not shown) appears similar to that shown in Figures 1 and 2, displaced by the mean jet location for this period at about 13°N .

[41] Using the distinction between different cloud types listed in section 6, we focus on the frequency of cumulonimbus and congestus events in relation to the jet. Similar to the method introduced in section 4, for each CloudSat-CALIPSO overpass we group profiles per 0.5° latitude and calculate the fraction of profiles with the relevant cloud type (cumulonimbus or congestus). If this fraction exceeds a threshold of 10% (about 3 CloudSat-CALIPSO profiles per 0.5° latitude), we classify it as an event. Figure 7 shows the frequency distribution of cumulonimbus events for nighttime observations (Figure 7a) and daytime observations (Figure 7b) and congestus events for nighttime (Figure 7c) and daytime (Figure 7d) observations versus latitude and dynamic latitude. The frequency of congestus events exceeds 5% between 3°N and 15°N for night and day, which agrees with Figures 2a and 2b, but Figures 5a and 5b showed that the congestus cloud fraction exceeded 5% only during the day between 4°N and 10°N . These results imply that congestus are frequently observed, but they do not cover a large area when present. All distributions from Figure 7 highly resemble the probability density function for weak convective systems during the WAM derived from TRMM, fitted to a Gumbel distribution by Mohr and Thorncroft [2006]. In terms of the standard deviation for either congestus or cumulonimbus, only the daytime cumulonimbus distribution in Figure 7b has a narrower spread with respect to dynamic latitude compared to standard latitude, while the other distributions show an increase in standard deviation as we shift to dynamic latitude.

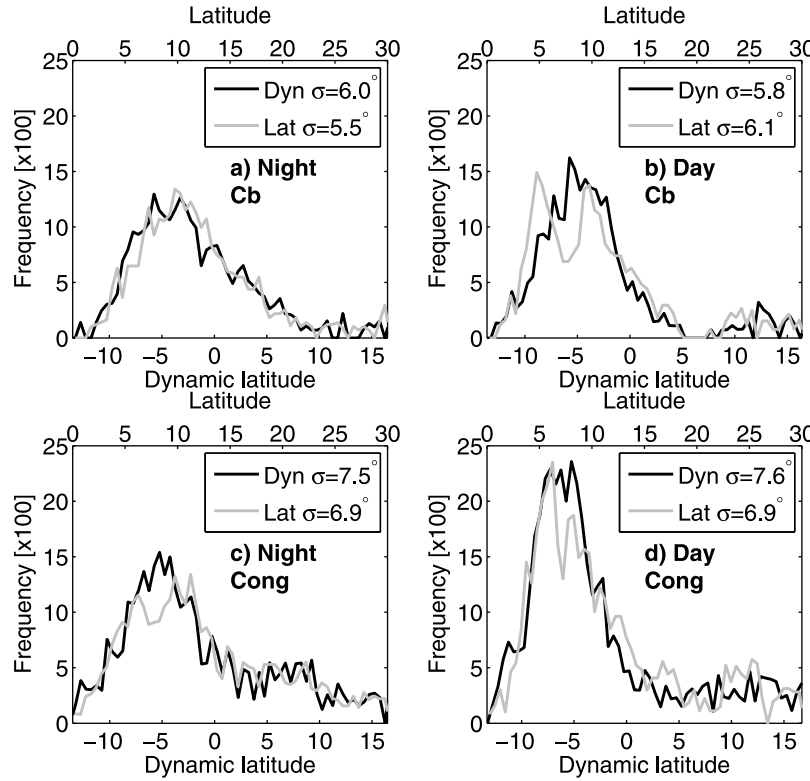


Figure 7. (a–b) Frequency of events with 10% cumulonimbus profiles or more for nighttime observations (Figure 7a) and daytime observations (Figure 7b), versus latitude (gray line and top x axis) and dynamic latitude (black line and bottom x axis), both in degrees north. (c–d) The same setup but for congestus events. The standard deviations for the distributions are provided in each legend.

[42] To illustrate the implications of the differences in standard deviation between the distributions in Figure 7, let us denote the correlation between event latitude ϕ and AEJ position δ by

$$\rho(\phi, \delta) = \frac{\text{Cov}(\phi, \delta)}{\sigma(\phi)\sigma(\delta)}, \quad (1)$$

where we can calculate the covariance “Cov” and standard deviations σ from the distributions of event frequency and AEJ locations. Assuming the hypothesis that the location of convective systems is related to the AEJ location, a northward (positive) displacement of the jet would be combined with a northward (positive) displacement of convective events, so a positive correlation $\rho(\phi, \delta)$. If the AEJ had no control over convection during the WAM, then $\rho(\phi, \delta) = 0$ and we would simply be adding variance from the jet position to the distributions by latitude in Figure 7, thus increasing the standard deviation:

$$\sigma(\phi - \delta) = \sqrt{\sigma^2(\phi) + \sigma^2(\delta) - 2\text{Cov}(\phi, \delta)}, \quad (2)$$

where $\sigma(\phi - \delta)$ is the standard deviation for cloud dynamic latitude, and $\text{Cov}(\phi, \delta) = 0$ if $\rho(\phi, \delta) = 0$. The AEJ position calculated from the analyses has a standard deviation of 2.8° at 00:00 UTC, while at 12:00 UTC we find $\sigma(\delta) = 2.7^\circ$. Using the values for $\sigma(\phi - \delta)$ and $\sigma(\phi)$ given in Figure 7, we find $\rho(\phi, \delta)$ near 0 for congestus and nighttime cumulonimbus, whereas for daytime cumulonimbus $\rho(\phi, \delta) = 0.33$.

Similarly, we can calculate the correlation between the dynamic latitude of convective events and AEJ position, and find $\rho(\phi - \delta, \delta) \approx -0.40$ for congestus and nighttime cumulonimbus, with $\rho(\phi - \delta, \delta) = -0.12$ for daytime cumulonimbus.

[43] The result for daytime cumulonimbus indicates that on average, such events occur more frequently farther north as the AEJ moves northward for $\rho(\phi, \delta) > 0$, but their mean shift is not as far north as that of the jet since $\rho(\phi - \delta, \delta) < 0$. Peaks of daytime cumulonimbus frequency can be seen at 5°N and at 10°N , similar to the cloud columns of Figure 1b associated with the Cameroon Highlands and the Jos Plateau, respectively. This strong preference of daytime cumulonimbus for orographic regions tied with its positive correlation with the jet position encourages further investigation into the interplay between the AEJ dynamics and local orographic forcing of convection in the WAM. The correlations observed for the other event frequencies ($\rho(\phi, \delta) \approx 0$) does not imply there is no value in studying convection in relation to the jet. There is clearly a steep decline in frequency of daytime (and nighttime) congestus events from almost 25% (15%) around 5° south of the jet to 5% at the jet location. Similarly, the frequency of nighttime cumulonimbus events drops from over 10% just south of the jet to 5% at 5° north of the jet.

[44] In this study we assumed that the AEJ position has a stable long-term mean around which deviations or African easterly wave disturbances occur. However, the mean jet position actually varies during the WAM, reaching its

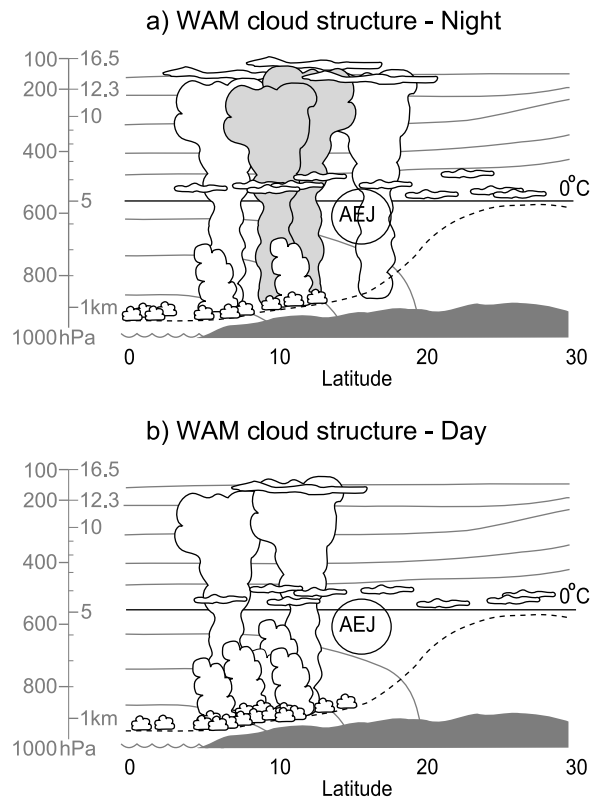


Figure 8. A schematic diagram of the WAM zonal mean vertical cloud structure observed by CloudSat and CALIPSO for (a) nighttime (01:30 LT) and (b) daytime (13:30 LT) observations, with pressure as vertical coordinate. A thick solid line indicates the daily mean position of the freezing level, thin gray solid lines are daily mean contours of constant potential temperature, and a closed contour indicates the average location of the AEJ, all taken from Figure 5. A dashed line indicates the depth of the mixing layer and is taken from *Parker et al.* [2005a, Figure 10] and *Cuesta et al.* [2009, Figure 1]. Land is shaded dark gray and follows the surface pressure contour of Figure 1 to indicate mean orography. Clouds are shown where they are frequently observed. Cumulonimbus (with anvil) are shaded light gray to indicate a high mean amount when present. Heights above mean sea level are indicated at 1 km spacing on the pressure axis for reference.

northernmost position usually in August. Furthermore, the zonal approximation of the cloud and precipitation structure ignores highly localized regions of convection such as the Cameroon and Guinea highlands [*Mohr and Thorncroft*, 2006]. Unfortunately, CloudSat-CALIPSO observations are too infrequent in time and too sparse in the longitudinal direction to provide better statistics on such regional and synoptic-scale variations. Therefore, for more definitive answers on the AEJ as a control on convection, we should revert to the more regular and wider coverage from instruments such as SEVIRI or TRMM.

8. Discussion and Conclusions

[45] This paper describes the vertical distribution of clouds in the WAM system using observations from

CloudSat and CALIPSO, with an emphasis on different cloud types, distinguished in the satellite data according to thresholds related to physical processes (e.g., detrainment above freezing level) and according to minima in the observed distributions of cloud frequency. Here, the results have been organized according to latitude, according to position relative to the AEJ, and according to month in the season. This has enabled us to study the north-south progression of key cloud types including nonprecipitating forms such as cirrus, cumulus congestus, altocumulus, and shallow cumulus, which through radiative feedbacks and through their role in the regional water cycle have a major impact on the seasonal and regional climate.

[46] Our main result can be summarized by providing a new analysis of cloud occurrences during the WAM in Figures 3, 4, and 5 that generalizes the schematic of *Parker et al.* [2005a]; a revised cloud structure for the WAM is shown in Figure 8 as a guide to the following conclusions. Nocturnal stratus is observed over the Gulf of Guinea at 01:30 LT, possibly driven northward over land [*Schrage et al.*, 2007] to provide the moisture inflow for shallow convection and congestus in the early afternoon at 13:30 LT [*Lothon et al.*, 2008]. The combination of CloudSat-CALIPSO observations clearly show an altocumulus layer stretching from roughly near the coastline northward through the region of deep convection, where it is likely caused by midlevel detrainment [*Johnson et al.*, 1999], toward and across the Sahara, where it is situated at the top of the SAL. The altocumulus layer is frequent both at day and at night and mostly topped by supercooled liquid, of which the presence is identified by a strong backscatter signal from the CALIPSO lidar [*Delanoë and Hogan*, 2010]. Deep convection, together with anvil, is confined to the region between 5°N and 15°N at night while during the day it is mostly associated with orographic regions at 5°N and 10°N. Cirrus is confined to the same latitudes, but with higher amounts toward the north, with planetary wave activity a possible explanation for this shift in location compared to the deep convective region [*Virts and Wallace*, 2010]. The AEJ is shown to have value as a marker for deep convection, as nighttime deep convective cloud fractions above 5% extend just north of the jet for all months, while for daytime convection this is only true for August and September. A separate analysis of the event frequency versus dynamic latitude of congestus and cumulonimbus shows a dropoff in the frequency for both these cloud types at day and night from maxima above 10% around 5° south of the AEJ to values of 5% and lower at the jet location, while the shape of the congestus and cumulonimbus frequency distributions agrees with results from *Mohr and Thorncroft* [2006] using TRMM observations. This quantification of the schematic in Figure 10 from *Parker et al.* [2005a] with observations from CloudSat and CALIPSO strongly supports the trimodal concept of tropical convection [*Johnson et al.*, 1999] within the meridional and diurnal variation of the WAM.

[47] These results present some challenging tasks for both numerical weather prediction and climate models. The separation of cloud fraction into frequency of occurrence and amount when present on a typical climate model resolution provides an immediate benchmark for model evaluation [*Hogan et al.*, 2001] and is relevant to further our understanding of the radiative balance. The prevalence of

Saharan altocumulus requires the assessment of the radiative impact of these clouds as well as capability of models to represent their microphysics correctly. In particular, the interaction between dust and the supercooled liquid in these clouds will change their properties by ice nucleation and possibly cause precipitation [Ansmann et al., 2008]. Finally, all cloud types and not just the deep convective storms show diurnal variation as well as monthly progression with the monsoon and accurate representation of these cloud developments will improve the water cycle in future models.

[48] **Acknowledgments.** We thank the ICARE Data and Services Center for their assistance, development support, and data processing for the CloudSat-CALIPSO merged product, DARDAR-MASK, available from icare.univ-lille1.fr/projects/dardar. Official CloudSat products “2B-GEOPROF” and “ECMWF-AUX” are available at cloudsat.cira.colostate.edu and are provided by the NASA CloudSat project. CALIPSO lidar data are available at eosweb.larc.nasa.gov. T. H. M. Stein wishes to thank Chris Westbrook for further insight into supercooled liquid in midlevel clouds and Maarten Ambaum for fruitful discussions on the statistical analysis of the AEJ control on convection. Comments from Adrian Tompkins and two anonymous reviewers greatly improved this work. This work has been funded by NERC grants NE/E003826/1, NE/E00525X/1, AMMA-UK NE/B505538/1, and NE/G018499/1.

References

- Agustí-Panareda, A., A. Beljaars, C. Cardinali, I. Genkova, and C. Thorncroft (2010), Impacts of assimilating AMMA soundings on ECMWF analyses and forecasts, *Weather Forecasting*, **25**, 1142–1160.
- Allan, R. P., A. Slingo, S. F. Milton, and M. E. Brooks (2007), Evaluation of the Met Office global forecast model using Geostationary Earth Radiation Budget (GERB) data, *Q. J. R. Meteorol. Soc.*, **133**, 1993–2010.
- Anselmo, T., R. Clifton, W. Hunt, K. Lee, T. Murray, K. Powell, O. Chomette, M. Viollier, A. Garnier, and J. Pelon (2006), Cloud-Aerosol LIDAR Infrared Pathfinder Satellite Observations (CALIPSO), in *Data Management System and Data Products Catalog*, Doc. PC-SCI-503, NASA, Hampton, Va.
- Ansmann, A., et al. (2008), Influence of Saharan dust on cloud glaciation in southern Morocco during the Saharan Mineral Dust Experiment, *J. Geophys. Res.*, **113**, D04210, doi:10.1029/2007JD008785.
- Battaglia, A., J. M. Haynes, T. L'Ecuyer, and C. Simmer (2008), Identifying multiple-scattering-affected profiles in CloudSat observations over the oceans, *J. Geophys. Res.*, **113**, D00A17, doi:10.1029/2008JD009960.
- Ben-Ami, Y., I. Koren, and O. Altartaz (2009), Patterns of North African dust transport over the Atlantic: Winter vs. summer, based on CALIPSO first year data, *Atmos. Chem. Phys.*, **9**, 7867–7875.
- Betts, A. K. (1986), A new convective adjustment scheme, Part I: Observational and theoretical basis, *Q. J. R. Meteorol. Soc.*, **112**, 677–691.
- Cornforth, R. J., B. J. Hoskins, and C. D. Thorncroft (2009), The impact of moist processes on the African easterly jet–African easterly wave system, *Q. J. R. Meteorol. Soc.*, **135**, 894–913.
- Cuesta, J., J. H. Marsham, D. J. Parker, and C. Flamant (2009), Dynamical mechanisms controlling the vertical redistribution of dust and the thermodynamic structure of the West Saharan atmospheric boundary layer during summer, *Atmos. Sci. Lett.*, **10**, 34–42.
- Dee, D. P., et al. (2011), The ERA-Interim reanalysis: Configuration and performance of the data assimilation system, *Q. J. R. Meteorol. Soc.*, **137**, 553–597.
- Delanoë, J., and R. J. Hogan (2010), Combined CloudSat-CALIPSO-MODIS retrievals of the properties of ice clouds, *J. Geophys. Res.*, **115**, D00H29, doi:10.1029/2009JD012346.
- Duvel, J. P. (1988), Analysis of diurnal, interdiurnal and interannual variations during Northern Hemisphere summers using METEOSAT infrared channels, *J. Clim.*, **1**, 471–484.
- Duvel, J. P. (1989), Convection over tropical Africa and the Atlantic Ocean during northern summer, Part I: Interannual and diurnal variations, *Mon. Weather Rev.*, **117**, 2782–2799.
- Fink, A. H., and A. Reiner (2003), Spatiotemporal variability of the relation between African easterly waves and West African squall lines in 1998 and 1999, *J. Geophys. Res.*, **108**(D11), 4332, doi:10.1029/2002JD002816.
- Geerts, B., and T. Dejene (2005), Regional and diurnal variability of the vertical structure of precipitation systems in Africa based on spaceborne radar data, *J. Clim.*, **18**, 893–916.
- Hamilton, R. A., and J. W. Archbold (1945), Meteorology of Nigeria and adjacent territory, *Q. J. R. Meteorol. Soc.*, **71**, 231–264.
- Hodges, K. I., and C. D. Thorncroft (1997), Distribution and statistics of African mesoscale convective weather systems based on ISCCP Meteorol. imagery, *Mon. Weather Rev.*, **125**, 2821–2837.
- Hogan, R. J., C. Jakob, and A. J. Illingworth (2001), Comparison of ECMWF winter-season cloud fraction with radar-derived values, *J. Appl. Met.*, **40**, 513–525.
- Hogan, R. J., M. D. Behera, E. J. O'Connor, and A. J. Illingworth (2004), Estimate of the global distribution of stratiform supercooled liquid water clouds using the LITE lidar *Geophys. Res. Lett.*, **31**, L05106, doi:10.1029/2003GL018977.
- Hopsch, S. B., C. D. Thorncroft, and K. R. Tyle (2010), Analysis of African easterly wave structures and their role in influencing tropical cyclogenesis, *Mon. Weather Rev.*, **138**, 1399–1419.
- Intergovernmental Panel on Climatic Change (IPCC) (2007), *Climate Change 2007: The Physical Science Basis: Contribution of Working Group I to the Fourth Assessment Report of the Intergovernmental Panel on Climate Change*, Sect. 10.3.5.2, edited by S. Solomon et al., Cambridge Univ. Press, Cambridge, U. K.
- Johnson, R. H., P. E. Ciesielski, and K. A. Hart (1996), Tropical inversions near the 0°C level, *J. Atmos. Sci.*, **53**, 1838–1855.
- Johnson, R. H., T. M. Rickenbach, S. A. Rutledge, P. E. Ciesielski, and W. H. Schubert (1999), Trimodal characteristics of tropical convection, *J. Clim.*, **12**, 2397–2418.
- Laing, A. G., R. Carbone, V. Levizzani, and J. Tuttle (2008), The propagation and diurnal cycles of deep convection in northern tropical Africa, *Q. J. R. Meteorol. Soc.*, **134**, 93–109.
- Landsea, C. W. (1993), A climatology of intense (or major) Atlantic hurricanes, *Mon. Weather Rev.*, **121**, 1703–1713.
- Lothon, M., F. Saïd, F. Lohou, and B. Campistron (2008), Observation of the diurnal cycle in the low troposphere of West Africa, *Mon. Weather Rev.*, **136**, 3477–3500.
- Luo, Z., G. Y. Liu, G. L. Stephens, and R. H. Johnson (2009), Terminal versus transient cumulus congestus: A CloudSat perspective, *Geophys. Res. Lett.*, **36**, L05808, doi:10.1029/2008GL036927.
- Mace, G. G., Q. Zhang, M. Vaughn, R. Marchand, G. Stephens, C. Trepte, and D. Winker (2009), A description of hydrometeor layer occurrence statistics derived from the first year of merged CloudSat and CALIPSO data, *J. Geophys. Res.*, **114**, D00A26, doi:10.1029/2007JD009755.
- Marchand, R., G. G. Mace, T. Ackerman, and G. Stephens (2008), Hydrometeor detection using CloudSat: An Earth-orbiting 94-GHz cloud radar, *J. Atmos. Oceanic Technol.*, **25**, 519–533.
- Marsham, J. H., D. J. Parker, C. M. Grams, C. M. Taylor, and J. M. Haywood (2008), Uplift of Saharan dust south of the intertropical discontinuity, *J. Geophys. Res.*, **113**, D21102, doi:10.1029/2008JD009844.
- Mathon, V., H. Laurent, and T. Lebel (2002), Mesoscale convective system rainfall in the Sahel, *J. Appl. Meteorol.*, **41**, 1081–1092.
- Meynadier, R., O. Bock, F. Guichard, A. Boone, P. Roucou, and J.-L. Redelsperger (2010), West African monsoon water cycle: 1. A hybrid water budget data set, *J. Geophys. Res.*, **115**, D19106, doi:10.1029/2010JD013917.
- Milton, S. F., G. Greed, M. E. Brooks, J. Haywood, B. Johnson, R. P. Allan, A. Slingo, and W. M. F. Grey (2008), Modeled and observed atmospheric radiation balance during the West African dry season: Role of mineral dust, biomass burning aerosol, and surface albedo, *J. Geophys. Res.*, **113**, D00C02, doi:10.1029/2007JD009741.
- Mohr, K. I. (2004), Interannual, monthly, and regional variability in the wet season diurnal cycle of precipitation in sub-Saharan Africa, *J. Clim.*, **17**, 2441–2453.
- Mohr, K. I., and C. D. Thorncroft (2006), Intense convective systems in West Africa and their relationship to the African easterly jet, *Q. J. R. Meteorol. Soc.*, **132**, 163–176.
- Newell, R. E., and J. W. Kidson (1984), African mean wind changes between Sahelian wet and dry periods, *J. Climatol.*, **4**, 27–33.
- Parker, D. J., C. D. Thorncroft, R. R. Burton, and A. Diongue-Niang (2005a), Analysis of the African easterly jet, using aircraft observations from the JET2000 experiment, *Q. J. R. Meteorol. Soc.*, **131**, 1461–1482.
- Parker, D. J., R. R. Burton, A. Diongue-Niang, R. J. Ellis, M. Felton, C. M. Taylor, C. D. Thorncroft, P. Bessemoulin, and A. M. Tompkins (2005b), The diurnal cycle of the West African monsoon circulation, *Q. J. R. Meteorol. Soc.*, **131**, 2839–2860.
- Partain, P. (2007), CloudSat ECMWF-AUX Auxiliary Data Process Description and Interface Control Document, technical report, Coop. Inst. for Res. in the Atmos., Colo. State Univ., Fort Collins.
- Redelsperger, J.-L., C. D. Thorncroft, A. Diedhiou, T. Lebel, D. J. Parker, and J. Polcher (2006), African monsoon multidisciplinary analysis: An international research project and field campaign, *Bull. Am. Meteorol. Soc.*, **87**, 1739–1746.

- Rodwell, M. J., and T. Jung (2008), Understanding the local and global impacts of model physics changes: An aerosol example, *Q. J. R. Meteorol. Soc.*, **134**, 1479–1497.
- Schrage, J. M., S. Augustyn, and A. H. Fink (2007), Nocturnal stratiform cloudiness during the West African monsoon, *Meteorol. Atmos. Phys.*, **95**, 73–86.
- Stein, T. H. M., J. Delanoë, and R. J. Hogan (2011), A comparison among four different retrieval methods for ice-cloud properties using data from CloudSat, CALIPSO, and MODIS, *J. Appl. Meteorol. Climatol.*, **50**, 1052–1069.
- Stephens, G. L., et al. (2002), The CloudSat mission and the A-Train, *Bull. Am. Meteorol. Soc.*, **83**, 1771–1790.
- Sultan, B., and S. Janicot (2003a), The West African monsoon dynamics, Part I: Documentation of intraseasonal variability, *J. Clim.*, **16**, 3389–3406.
- Sultan, B., and S. Janicot (2003b), The West African monsoon dynamics, Part II: The “preonset” and “onset” of the summer monsoon, *J. Clim.*, **16**, 3407–3427.
- Sultan, B., S. Janicot, and P. Drobinski (2007), Characterization of the diurnal cycle of the West African monsoon around the monsoon onset, *J. Clim.*, **20**, 4014–4032.
- Thorncroft, C. D., and M. Blackburn (1999), Maintenance of the African easterly jet, *Q. J. R. Meteorol. Soc.*, **125**, 763–786.
- Thorncroft, C. D., and K. Hodges (2001), African easterly wave variability and its relationship to Atlantic tropical cyclone activity, *J. Clim.*, **14**, 1166–1179.
- Thorncroft, C. D., et al. (2003), The JET2000 project: Aircraft observations of the African easterly jet and African easterly waves, *Bull. Am. Meteorol. Soc.*, **84**, 337–351.
- Tompkins, A. M., C. Cardinali, J.-J. Morcrette, and M. Rodwell (2005a), Influence of aerosol climatology on forecasts of the African easterly jet, *Geophys. Res. Lett.*, **32**, L10801, doi:10.1029/2004GL022189.
- Tompkins, A. M., A. Diongue-Niang, D. J. Parker, and C. D. Thorncroft (2005b), The African easterly jet in the ECMWF Integrated Forecast System: 4D-Var analysis, *Q. J. R. Meteorol. Soc.*, **131**, 2861–2885.
- Virts, K. S., and J. M. Wallace (2010), Annual, interannual, and intraseasonal variability of tropical tropopause transition layer cirrus, *J. Atmos. Sci.*, **67**, 3097–3112.
- Wang, Z., and K. Sassen (2007), Level 2 Cloud Scenario Classification Product Process Description and Interface Control Document, technical report, Coop. Inst. for Res. in the Atmos., Colo. State Univ., Fort Collins.
- Westbrook, C. D., and A. J. Illingworth (2011), Evidence that ice forms primarily in supercooled liquid clouds at temperatures $>-27^{\circ}\text{C}$, *Geophys. Res. Lett.*, **38**, L14808, doi:10.1029/2011GL048021.
- Winker, D. M., J. Pelon, and M. P. McCormick (2003), The CALIPSO mission: Spaceborne lidar for observation of aerosols and clouds, in *Proc. SPIE Int. Soc. Opt. Eng.*, **4893**, 1–11.
- J. Delanoë, LATMOS/IPSL/UVSQ, 11 D’Alembert, Guyancourt F-78280, France. (julien.delanoe@latmos.ipsl.fr)
- N. S. Dixon, P. Knippertz, J. H. Marsham, and D. J. Parker, Institute for Climate and Atmospheric Science, School of Earth and Environment, University of Leeds, Leeds LS2 9JT, UK. (n.s.dixon@leeds.ac.uk; p.knippertz@leeds.ac.uk; j.marsham@leeds.ac.uk; d.j.parker@leeds.ac.uk)
- R. J. Hogan, R. I. Maidment, and T. H. M. Stein, Department of Meteorology, University of Reading, Earley Gate, PO Box 243, Reading RG6 6BB, UK. (r.j.hogan@reading.ac.uk; r.i.maidment@pgr.reading.ac.uk; t.h.m.stein@reading.ac.uk)